

# H<sub>2</sub>CO in the Horsehead PDR: Photo-desorption of dust grain ice mantles

V. Guzmán<sup>1,2</sup>, J. Pety<sup>2,1</sup>, J.R. Goicoechea<sup>3</sup>, M. Gerin<sup>1</sup>, and E. Roueff<sup>4</sup>

<sup>1</sup> LERMA - LRA, UMR 8112, Observatoire de Paris and Ecole normale Supérieure, 24 rue Lhomond, 75231 Paris, France.  
e-mail: [viviana.guzman;maryvonne.gerin]@lra.ens.fr

<sup>2</sup> IRAM, 300 rue de la Piscine, 38406 Grenoble Cedex, France.  
e-mail: pety@iram.fr

<sup>3</sup> Departamento de Astrofísica. Centro de Astrobiología. CSIC-INTA. Carretera de Ajalvir, Km 4. Torrejón de Ardoz, 28850 Madrid, Spain.  
e-mail: jr.goicoechea@cab.inta-csic.es

<sup>4</sup> LUTH UMR 8102, CNRS and Observatoire de Paris, Place J. Janssen, 92195 Meudon Cedex, France.  
e-mail: evelyne.roueff@obspm.fr

Received May 16, 2011; accepted August 22, 2011

## ABSTRACT

**Aims.** For the first time we investigate the role of the grain surface chemistry in the Horsehead Photo-dissociation region (PDR).

**Methods.** We performed deep observations of several H<sub>2</sub>CO rotational lines toward the PDR and its associated dense-core in the Horsehead nebula, where the dust is cold ( $T_{\text{dust}} \approx 20-30$  K). We complemented these observations with a map of the p-H<sub>2</sub>CO  $3_{03}-2_{02}$  line at 218.2 GHz (with 12'' angular resolution). We determine the H<sub>2</sub>CO abundances using a detailed radiative transfer analysis and compare these results with PDR models that include either pure gas-phase chemistry or both gas-phase and grain surface chemistry.

**Results.** The H<sub>2</sub>CO abundances ( $\approx 2-3 \times 10^{-10}$ ) with respect to H-nuclei are similar in the PDR and dense-core. In the dense-core the pure gas-phase chemistry model reproduces the observed H<sub>2</sub>CO abundance. Thus, surface processes do not contribute significantly to the gas-phase H<sub>2</sub>CO abundance in the core. In contrast, the formation of H<sub>2</sub>CO on the surface of dust grains and subsequent photo-desorption into the gas-phase are needed in the PDR to explain the observed gas-phase H<sub>2</sub>CO abundance, because the gas-phase chemistry alone does not produce enough H<sub>2</sub>CO. The assignments of different formation routes are strengthened by the different measured ortho-to-para ratio of H<sub>2</sub>CO: the dense-core displays the equilibrium value ( $\sim 3$ ) while the PDR displays an out-of-equilibrium value ( $\sim 2$ ).

**Conclusions.** Photo-desorption of H<sub>2</sub>CO ices is an efficient mechanism to release a significant amount of gas-phase H<sub>2</sub>CO into the Horsehead PDR.

**Key words.** Astrochemistry – ISM: clouds – ISM: molecules – ISM: individual objects: Horsehead nebula – Radiative transfer – Radio lines: ISM

## 1. Introduction

Photo-dissociation region (PDR) models are used to understand the evolution of the far-UV illuminated matter both in our Galaxy and in external galaxies. The spectacular instrumental improvements, which happen in radioastronomy with the advent of Herschel, ALMA and NOEMA, call for matching progresses in PDR modeling. In particular, the physics and chemistry of the dust grains and of the gas-phase are intricately intertwined. It is well known that the formation of ice grain mantles leads to the removal of chemical reservoirs like CO, O, and other abundant species from the gas phase, enabling new chemical routes to be opened and others to be closed. Despite their low temperature, the mantles are chemically active. Hydrogenation/deuteration reactions are known to be efficient, because hydrogen (or deuterium atoms) can migrate on the surfaces, but reactions with O, N, and C must also be considered. Complex molecules may therefore be formed before they are released into the gas phase. Moreover, the release of the products into the gas phase happens either through thermal processes (evaporation) or non-thermal ones (cosmic ray or far-UV photon-induced desorption). Recent photo-desorption experiments on water and CO ices show that this mechanism is much more efficient than pre-

viously thought (Öberg et al. 2009b,a; Muñoz Caro et al. 2010). These results led various groups to include photo-desorption into PDR models (see the results on H<sub>2</sub>O and O<sub>2</sub> by Hollenbach et al. 2009; Walsh et al. 2010; Hassel et al. 2010). The availability of well-defined observations is essential here to distinguish between chemical assumptions about the significant grain surface processes, *i.e.*, adsorption, desorption, and diffusion. It is now confirmed that some interstellar species are mostly formed in the gas-phase (CO for instance), others on grains (CH<sub>3</sub>OH, Garrod et al. 2007), while the chemical routes for other complex species such as formaldehyde, are still debated because it is likely that solid and gas-phase processes are both needed.

Formaldehyde (H<sub>2</sub>CO) was the first organic molecule discovered in the interstellar medium (Snyder et al. 1969). It is a relatively simple organic molecule that can be formed in the gas-phase and on the surface of dust grains. In the warm gas, H<sub>2</sub>CO can trigger the formation of more complex organic molecules (Charnley et al. 1992). It is one of the most popular molecules used for studying the physical conditions of the gas in astrophysical sources. Indeed, it is a good probe of the temperature and density of the gas (Mangum & Wootten 1993). Owing to its large dipole moment (2.3 Debye), its

Table 1: Observation parameters for the maps shown in Fig. 1. The projection center of all maps is  $\alpha_{2000} = 05^h40^m54.27^s$ ,  $\delta_{2000} = -02^\circ28'00''$ .

Molecule	Transition	Frequency GHz	Instrument	Beam arcsec	PA °	Vel. Resol. km s <sup>-1</sup>	Int. Time hours	$T_{\text{sys}}$ K ( $T_{\text{A}}^*$ )	Noise K ( $T_{\text{mb}}$ )	Obs.date
	Continuum at 1.2 mm		30m/MAMBO	11.7 × 11.7	0	–	–	–	–	–
DCO <sup>+</sup>	3-2	216.112582	30m/HERA	11.4 × 11.4	0	0.11	1.5/2.0 <sup>a</sup>	230	0.10	2006 Mar
p-H <sub>2</sub> CO	3 <sub>03</sub> – 2 <sub>02</sub>	218.222190	30m/HERA	11.9 × 11.9	0	0.05	2.1/3.4 <sup>a</sup>	280	0.32	2008 Jan
HCO	1 <sub>0,1</sub> 3/2, 2 – 0 <sub>0,0</sub> 1/2, 1	86.670760	PdBI/C&D	6.69 × 4.39	16	0.20	6.5 <sup>b</sup>	150	0.09 <sup>c</sup>	2006-2007

<sup>a</sup> Two values are given for the integration time: the on-source time and the telescope time. <sup>b</sup> On-source time computed as if the source were always observed with six antennae. <sup>c</sup> The noise values quoted here are the noises at the mosaic phase center (mosaic noise is inhomogeneous because of the primary beam correction; it steeply increases at the mosaic edges).

Table 2: Observation parameters of the deep integrations of the o-H<sub>2</sub>CO and p-H<sub>2</sub>CO lines toward the PDR and the dense-core.

Position	Molecule	Transition	$\nu$ [GHz]	Line area K km s <sup>-1</sup>	Instrument	$F_{\text{eff}}$	$B_{\text{eff}}$	Int. Time hours	$T_{\text{peak}}$ K ( $T_{\text{mb}}$ )	RMS K	S/N
PDR	o-H <sub>2</sub> CO	2 <sub>12</sub> – 1 <sub>11</sub>	140.839	1.75±0.02	30-m/C150	0.93	0.70	1.9	1.87	0.061	31
	p-H <sub>2</sub> CO	2 <sub>02</sub> – 1 <sub>01</sub>	145.603	1.32±0.02	30-m/D150	0.93	0.69	1.9	1.61	0.047	34
	o-H <sub>2</sub> CO	2 <sub>11</sub> – 1 <sub>10</sub>	150.498	1.41±0.02	30-m/C150	0.93	0.68	1.4	1.52	0.053	29
	o-H <sub>2</sub> CO	3 <sub>13</sub> – 2 <sub>12</sub>	211.211	1.24±0.03	30-m/B230	0.91	0.57	1.1	1.46	0.096	15
	p-H <sub>2</sub> CO	3 <sub>03</sub> – 2 <sub>02</sub>	218.222	0.77±0.01	30-m/B230	0.91	0.55	3.9	1.11	0.052	21
	p-H <sub>2</sub> CO	3 <sub>22</sub> – 2 <sub>21</sub>	218.476	0.17±0.01	30-m/B230	0.91	0.55	2.0	0.27	0.055	5
	o-H <sub>2</sub> CO	3 <sub>12</sub> – 2 <sub>11</sub>	225.698	0.84±0.02	30-m/A230	0.91	0.54	6.5	1.12	0.079	14
Dense-core	o-H <sub>2</sub> CO	2 <sub>12</sub> – 1 <sub>11</sub>	140.839	2.56±0.01	30-m/C150	0.93	0.70	3.7	3.46	0.036	96
	p-H <sub>2</sub> CO	2 <sub>02</sub> – 1 <sub>01</sub>	145.603	1.75±0.02	30-m/D150	0.93	0.69	1.9	2.62	0.044	60
	o-H <sub>2</sub> CO	2 <sub>11</sub> – 1 <sub>10</sub>	150.498	1.89±0.01	30-m/C150	0.93	0.68	1.5	2.52	0.052	49
	o-H <sub>2</sub> CO	3 <sub>13</sub> – 2 <sub>12</sub>	211.211	1.93±0.02	30-m/B230	0.91	0.57	2.0	3.02	0.065	47
	p-H <sub>2</sub> CO	3 <sub>03</sub> – 2 <sub>02</sub>	218.222	1.03±0.01	30-m/B230	0.91	0.55	3.0	1.83	0.057	32
	p-H <sub>2</sub> CO	3 <sub>22</sub> – 2 <sub>21</sub>	218.476	0.04±0.01	30-m/B230	0.91	0.55	4.5	0.06	0.037	2
	o-H <sub>2</sub> CO	3 <sub>12</sub> – 2 <sub>11</sub>	225.698	1.27±0.02	30-m/A230	0.91	0.54	8.4	1.96	0.073	27
	o-H <sub>2</sub> <sup>13</sup> CO	2 <sub>12</sub> – 1 <sub>11</sub>	137.450	0.09±0.02	30-m/D150	0.95	0.70	2.0	0.11	0.063	2
	p-H <sub>2</sub> <sup>13</sup> CO	2 <sub>02</sub> – 1 <sub>01</sub>	141.984	0.10±0.01	30-m/D150	0.95	0.70	1.5	0.11	0.060	2
	HDCO	2 <sub>11</sub> – 1 <sub>10</sub>	134.285	0.13±0.01	30-m/C150	0.94	0.71	2.0	0.32	0.042	8
	HDCO	3 <sub>12</sub> – 2 <sub>11</sub>	201.341	0.05±0.01	30-m/A230	0.91	0.59	3.5	0.13	0.032	4
p-D <sub>2</sub> CO	2 <sub>12</sub> – 1 <sub>11</sub>	110.838	0.04±0.01	30-m/A100	0.95	0.75	4.9	0.08	0.031	3	
o-D <sub>2</sub> CO	4 <sub>04</sub> – 3 <sub>03</sub>	231.410	0.04±0.01	30-m/A230	0.91	0.53	4.5	0.09	0.068	1	

rotational lines are easy to detect from ground-based observations. It is present in a variety of environments, such as Galactic HII regions (e.g., Downes et al. 1980), proto-stellar cores (e.g., Young et al. 2004; Maret et al. 2004), young stellar objects (e.g., Araya et al. 2007), PDRs (e.g., Leurini et al. 2010), starburst galaxies (e.g., Mangum et al. 2008) and comets (e.g., Snyder et al. 1989; Milam et al. 2006).

The Horsehead PDR is particularly well-suited to investigate grain surface chemistry in a UV irradiated environment. It is viewed nearly edge-on (Habart et al. 2005) at a distance of 400 pc (implying that 10'' correspond to 0.02 pc). Thus, it is possible to study the interaction of far-UV radiation with dense interstellar clouds and the transition from warm to cold gas in a PDR with a simple geometry, very close to the prototypical kind of source needed to serve as a reference to chemical models. Its relatively low UV illumination ( $\chi = 60$  in Draine units, Draine 1978) and high density ( $n_{\text{H}} \sim 10^4 - 10^5 \text{ cm}^{-3}$ ) implies low dust grain temperatures, from  $T_{\text{dust}} \sim 30$  K in the PDR to  $T_{\text{dust}} \sim 20$  K deeper inside the cloud (Goicoechea et al. 2009a). The release of the grain mantle products into the gas phase is consequently dominated by photo-desorption, while regions with warmer dust (the Orion bar or the star-forming cores) provide mixed information on the thermal and non-thermal processes (e.g., Bisschop et al. 2007).

In this paper we present deep observations of several formaldehyde lines toward two particular positions in the Horsehead nebula: the PDR, corresponding to the peak of the HCO emission (Gerin et al. 2009), where the gas is warm ( $T_{\text{kin}} \sim 60$  K); and the dense-core, a cold ( $T_{\text{kin}} \leq 20$  K) condensation located less than 40'' away from the PDR edge, where HCO<sup>+</sup> is highly deuterated (Pety et al. 2007). We present the observations and data reduction in Sect. 2, while the results and abundances are given in Sect. 3. In Sect. 4 we present the H<sub>2</sub>CO chemistry and PDR modeling. A discussion is given in Sect. 5 and we conclude in Sect. 6.

## 2. Observations and data reduction

Tables 1 and 2 summarize the observation parameters for the data obtained with the IRAM-30m and PdBI telescopes. Fig. 1 displays the p-H<sub>2</sub>CO, HCO, DCO<sup>+</sup> and 1.2 mm continuum maps. The p-H<sub>2</sub>CO line was mapped during 3.3 hours of good winter weather ( $\sim 1$  mm of water vapor) using the first polarization (*i.e.* nine of the eighteen available pixels) of the IRAM-30m/HERA single-sideband multi-beam receiver. We used the frequency-switched, on-the-fly observing mode. We observed along and perpendicular to the direction of the exciting star in zigzags (*i.e.*  $\pm$  the lambda and beta scanning direction). The

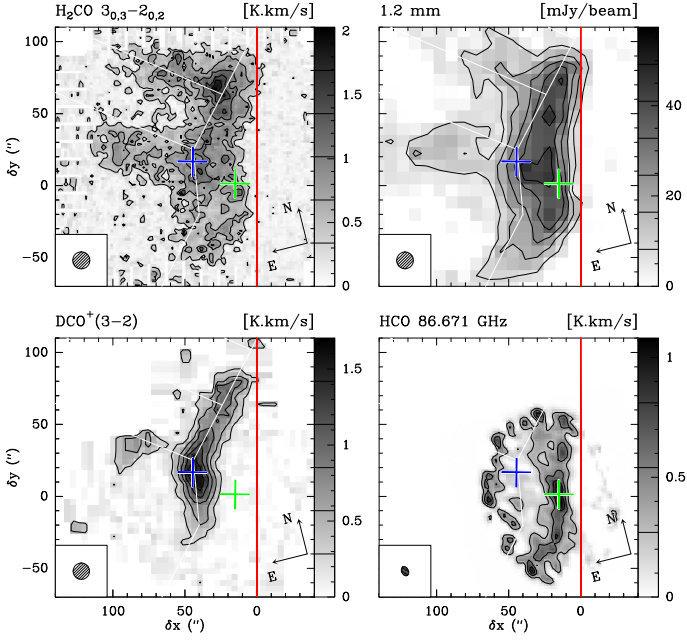


Fig. 1: Integrated intensity maps of the Horsehead edge. The intensities are expressed in the main-beam temperature scale. Maps were rotated by  $14^\circ$  counter-clockwise around the projection center, located at  $(\delta x, \delta y) = (20'', 0'')$ , to bring the exciting star direction in the horizontal direction and the horizontal zero was set at the PDR edge, delineated by the red vertical line. The crosses show the positions of the PDR (green) and the dense-core (blue), where deep integrations were performed at IRAM-30m (see Fig. 3). The spatial resolution is plotted in the bottom left corner. Values of contour levels are shown on each image lookup table. The emission of all lines is integrated between 10.1 and 11.1 km s<sup>-1</sup>.

multi-beam system was rotated by  $9.6^\circ$  with respect to the scanning direction. This ensured Nyquist sampling between the rows except at the edges of the map. The fully sampled part of the map covered a  $150'' \times 150''$  portion of the sky. A detailed description of the HCO, DCO<sup>+</sup> and 1.2 mm continuum observations and data reductions can be found in Gerin et al. (2009), Pety et al. (2007), and Hily-Blant et al. (2005).

We performed deep integrations of o-H<sub>2</sub>CO and p-H<sub>2</sub>CO low-energy rotational lines (see Fig. 2 and 3) centered on the PDR and the dense-core. To obtain these deep integration spectra, we used the position-switching observing mode. The on-off cycle duration was 1 minute and the off-position offsets were  $(\delta \text{RA}, \delta \text{Dec}) = (-100'', 0'')$ , *i.e.* the H II region ionized by  $\sigma$  Ori and free of molecular emission. From our knowledge of the IRAM-30m telescope we estimate the absolute position accuracy to be  $3''$ .

The data processing was made with the GILDAS<sup>1</sup> softwares (Pety 2005). The IRAM-30m data were first calibrated to the  $T_A^*$  scale using the chopper-wheel method (Penzias & Burrus 1973), and finally converted to main-beam temperatures ( $T_{\text{mb}}$ ) using the forward and main-beam efficiencies ( $F_{\text{eff}}$  &  $B_{\text{eff}}$ ) displayed in Table 2. The resulting amplitude accuracy is  $\sim 10\%$ . Frequency-switched spectra were folded using the standard shift-and-add method before baseline subtraction. The re-

<sup>1</sup> See <http://www.iram.fr/IRAMFR/GILDAS> for more information about the GILDAS softwares.

Table 3: Spectroscopic parameters of the observed lines obtained from the CDMS data base (Müller et al. 2001).

Molecule	Transition	$\nu$ [GHz]	$E_u$ [K]	$A_{ul}$ [s <sup>-1</sup> ]	$g_u$
o-H <sub>2</sub> CO	2 <sub>12</sub> – 1 <sub>11</sub>	140.839	21.92	$5.3 \times 10^{-5}$	15
p-H <sub>2</sub> CO	2 <sub>02</sub> – 1 <sub>01</sub>	145.603	10.48	$7.8 \times 10^{-5}$	5
o-H <sub>2</sub> CO	2 <sub>11</sub> – 1 <sub>10</sub>	150.498	22.62	$6.5 \times 10^{-5}$	15
o-H <sub>2</sub> CO	3 <sub>13</sub> – 2 <sub>12</sub>	211.211	32.06	$2.3 \times 10^{-4}$	21
p-H <sub>2</sub> CO	3 <sub>03</sub> – 2 <sub>02</sub>	218.222	20.96	$2.8 \times 10^{-4}$	7
p-H <sub>2</sub> CO	3 <sub>22</sub> – 2 <sub>21</sub>	218.476	68.09	$1.6 \times 10^{-4}$	7
o-H <sub>2</sub> CO	3 <sub>12</sub> – 2 <sub>11</sub>	225.698	33.45	$2.8 \times 10^{-4}$	21
o-H <sub>2</sub> <sup>13</sup> CO	2 <sub>12</sub> – 1 <sub>11</sub>	137.450	10.51	$4.9 \times 10^{-5}$	15
p-H <sub>2</sub> <sup>13</sup> CO	2 <sub>02</sub> – 1 <sub>01</sub>	141.984	2.37	$7.2 \times 10^{-5}$	5
HDCO	2 <sub>11</sub> – 1 <sub>10</sub>	134.285	17.63	$4.6 \times 10^{-5}$	5
HDCO	3 <sub>12</sub> – 2 <sub>11</sub>	201.341	27.29	$2.0 \times 10^{-4}$	7
o-D <sub>2</sub> CO	2 <sub>12</sub> – 1 <sub>11</sub>	110.838	13.37	$2.6 \times 10^{-5}$	5
p-D <sub>2</sub> CO	4 <sub>04</sub> – 3 <sub>03</sub>	231.410	27.88	$3.5 \times 10^{-4}$	18

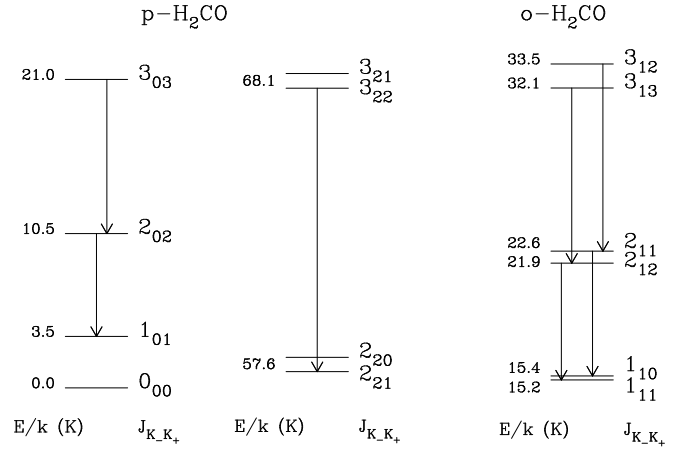


Fig. 2: Lower energy rotational levels of para- (left) and ortho-H<sub>2</sub>CO (right). The energy above para ground-state is shown to the left of each level. The arrows indicate the transitions detected in the Horsehead.

sulting spectra were finally gridded through convolution with a Gaussian to obtain the maps.

### 3. Results

#### 3.1. H<sub>2</sub>CO spatial distribution

The 218.2 GHz p-H<sub>2</sub>CO integrated line-intensity map is shown in Fig. 1 together with the 86.7 GHz HCO, 216.1 GHz DCO<sup>+</sup> integrated line-intensity maps and the 1.2 mm continuum-emission map. Formaldehyde emission is extended throughout the Horsehead with a relatively constant intensity. The H<sub>2</sub>CO spatial distribution resembles the 1.2 mm continuum emission: It follows the top of the famous Horsehead nebula from its front to its mane. It also delineates the throat of the Horsehead. The peak of the H<sub>2</sub>CO emission spatially coincides with the peak of the DCO<sup>+</sup> emission, which arises from a cold dense-core. However, H<sub>2</sub>CO emission is also clearly present along the PDR, which is traced by the HCO emission. The PDR and dense-core, namely the peaks of the HCO and DCO<sup>+</sup> emission are shown with green and blue crosses respectively. Gaussian fits of the

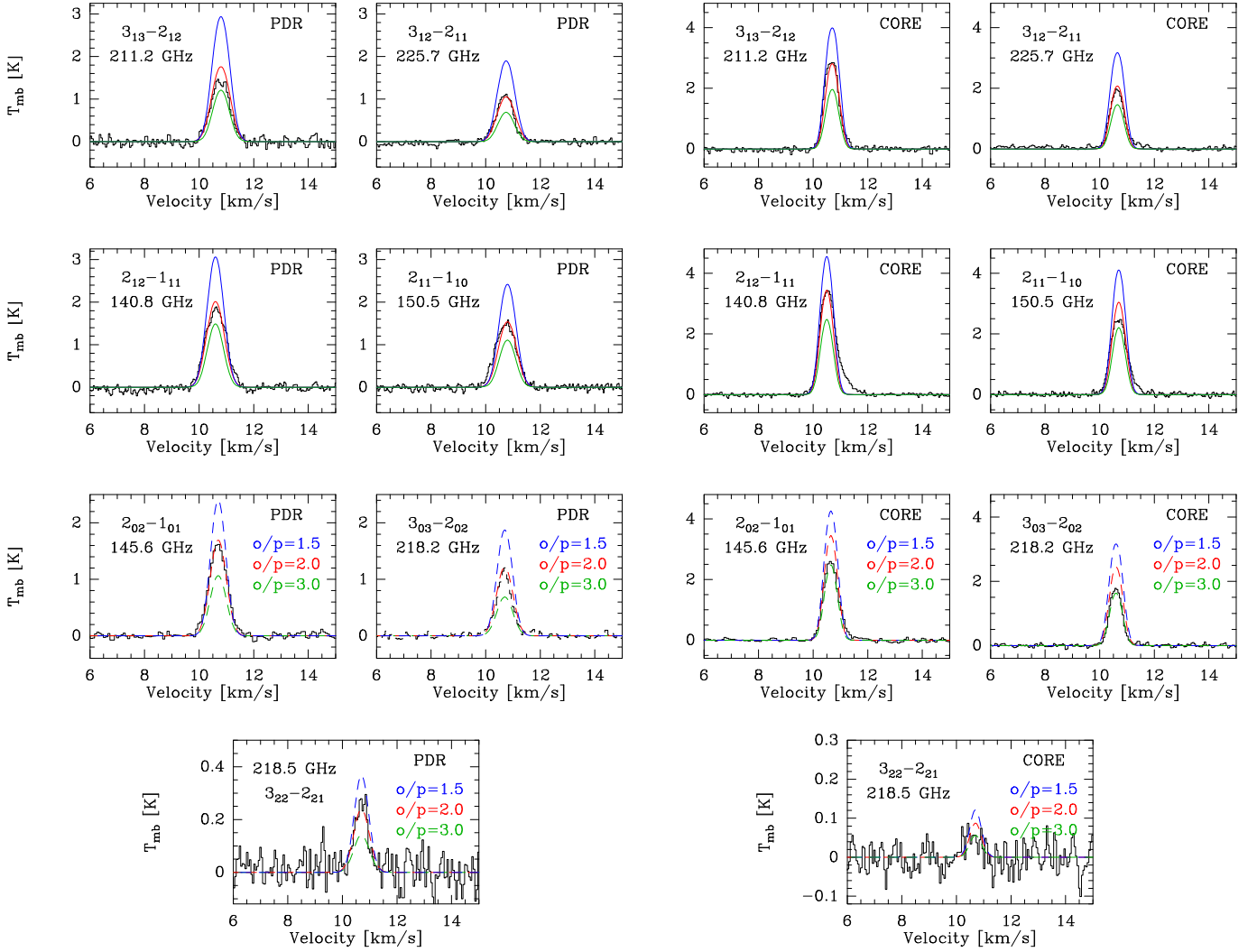


Fig. 3: Radiative transfer modeling of H<sub>2</sub>CO lines for two positions toward the Horsehead. Two left columns: the PDR position ( $T_{\text{kin}} = 60$  K,  $n(\text{H}_2) = 6 \times 10^4 \text{ cm}^{-3}$ ,  $N(\text{o-H}_2\text{CO}) = 7.2 \times 10^{12} \text{ cm}^{-2}$ ) and two right columns: the dense-core position ( $T_{\text{kin}} = 20$  K,  $n(\text{H}_2) = 10^5 \text{ cm}^{-3}$ ,  $N(\text{o-H}_2\text{CO}) = 9.6 \times 10^{12} \text{ cm}^{-2}$ ). The two top rows display the ortho lines, for which we varied the column density around the best match (red curve) by a factor of 1.5 (blue curve) and 1/1.5 (green curve). The two bottom rows display the para lines, for which we kept the column density of the best match for o-H<sub>2</sub>CO (red curves) constant and varied the ortho-to-para ratio of H<sub>2</sub>CO: o/p = 1.5 (dashed blue), o/p=2 (dashed red) and o/p=3 (dashed green)

H<sub>2</sub>CO lines at the HCO peak result in broader line widths than at the DCO<sup>+</sup> peak. That the lines are broader in the PDR confirms that H<sub>2</sub>CO lines toward the DCO<sup>+</sup> peak arise from the dense-core rather than from the illuminated surface of the cloud. There is a peak in the H<sub>2</sub>CO emission toward the north-west region of the nebula, near the edge of the PDR, where two protostars have been identified (B33-1 and B33-28, Bowler et al. 2009). These protostars heat the dust around them, so it is likely that H<sub>2</sub>CO has been evaporated from the grain ice mantles.

### 3.2. H<sub>2</sub>CO column density

We computed the column densities of H<sub>2</sub>CO at the PDR and the dense-core positions. For this we first used the H<sub>2</sub><sup>13</sup>CO lines to estimate the optical depth of the H<sub>2</sub>CO lines. Then, we made a first estimate of the column densities and excitation temperatures using rotational diagrams. Finally, we used these first estimates as an input for a detailed nonlocal non-LTE excitation and radiative transfer analysis to compute the H<sub>2</sub>CO abundances. The

spectroscopic parameters for the detected transitions (shown in Fig. 2) are given in Table 3. We assumed that the emission is extended and fills the 30m beam, as shown by the map of the 3<sub>03</sub> – 2<sub>02</sub> transition (see Fig. 1).

#### 3.2.1. Opacity of the H<sub>2</sub>CO lines

We detected two transitions of the formaldehyde isotopologue H<sub>2</sub><sup>13</sup>CO in the dense-core position (see upper panels in Fig. 4). By comparing the flux between H<sub>2</sub>CO and H<sub>2</sub><sup>13</sup>CO for the same transition it is possible to estimate the opacity of the H<sub>2</sub>CO line, assuming that the H<sub>2</sub><sup>13</sup>CO line is optically thin, as follows:

$$\frac{F_{\text{H}_2\text{CO}}}{F_{\text{H}_2^{13}\text{CO}}} = \frac{[^{12}\text{C}]}{[^{13}\text{C}]} \beta \quad (1)$$

where  $\beta$  is the escape probability function, which in the case of a homogeneous slab of gas (de Jong et al. 1980) is equal to

$$\beta = \frac{1 - \exp(-3\tau)}{3\tau} \quad (2)$$

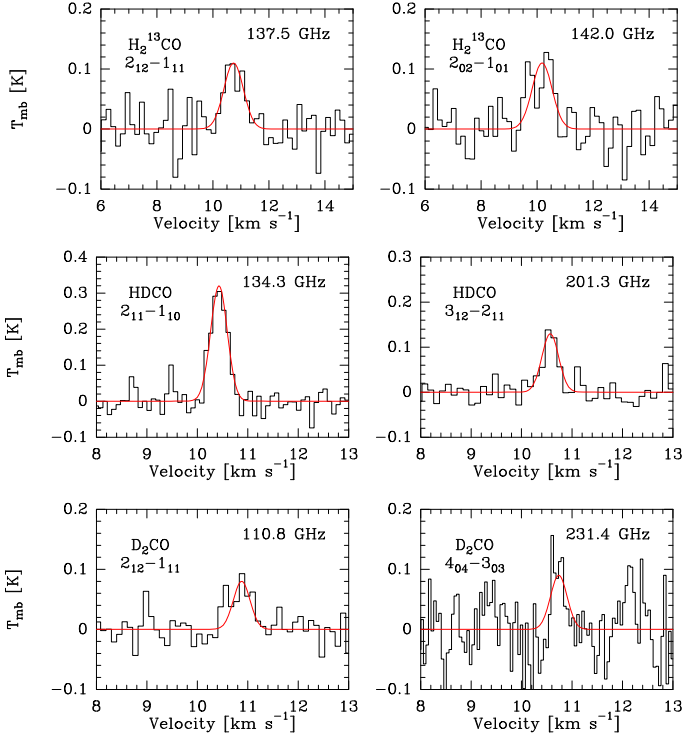


Fig. 4: H<sub>2</sub><sup>13</sup>CO and deuterated H<sub>2</sub>CO lines detected toward the dense-core. Gaussian fits are shown with red lines. For HDCO and D<sub>2</sub>CO the line width was fixed to the width of the HDCO (2<sub>11</sub> – 1<sub>10</sub>) line, because it has the best signal-to-noise ratio.

The isotopic abundance ratio <sup>12</sup>C/<sup>13</sup>C ≈ 60 (Langer & Penzias 1990; Savage et al. 2002) is almost twice the line intensity ratio between formaldehyde and its isotopologue, and therefore the H<sub>2</sub>CO lines have moderate opacities. From the observations we estimate τ<sub>2<sub>12</sub>-2<sub>11</sub></sub> ~ 1.6 and τ<sub>2<sub>02</sub>-1<sub>01</sub></sub> ~ 1.9 for H<sub>2</sub>CO in the dense-core.

### 3.2.2. Rotational diagram analysis

First-order estimates of the beam-averaged column densities and the rotational temperatures can be found by means of the widely used rotational diagram analysis (Goldsmith & Langer 1999). To do this, we assume that the gas is under LTE, and therefore all excitation temperatures are the same, and the energy levels are populated following Boltzmann’s law. We built rotational diagrams corrected for line-opacity effects through

$$\ln \frac{N_u^{\text{thin}}}{g_u} + \ln C_\tau = \ln \frac{N}{Z} - \frac{E_u}{kT_{\text{rot}}}, \quad (3)$$

where  $N$  is the total column density of the molecule,  $g_u$  is the level degeneracy,  $E_u/k$  is the energy of the upper level in K,  $Z$  is the partition function at the rotational temperature  $T_{\text{rot}}$ ,  $C_\tau = \frac{\tau}{1-e^{-\tau}} \leq 1$  is a line-opacity correction factor, where  $\tau$  is the opacity of the line, and  $N_u^{\text{thin}}$  is the column density of the upper level for an optically thin line when the source fills the beam. This last parameter is given by

$$N_u^{\text{thin}} = \frac{8\pi k\nu^2 W}{hc^3 A_{ul}}, \quad (4)$$

where  $k$  is the Boltzmann constant,  $\nu$  is the line frequency,  $W$  is the integrated line intensity,  $h$  is the Planck constant,  $c$  is the

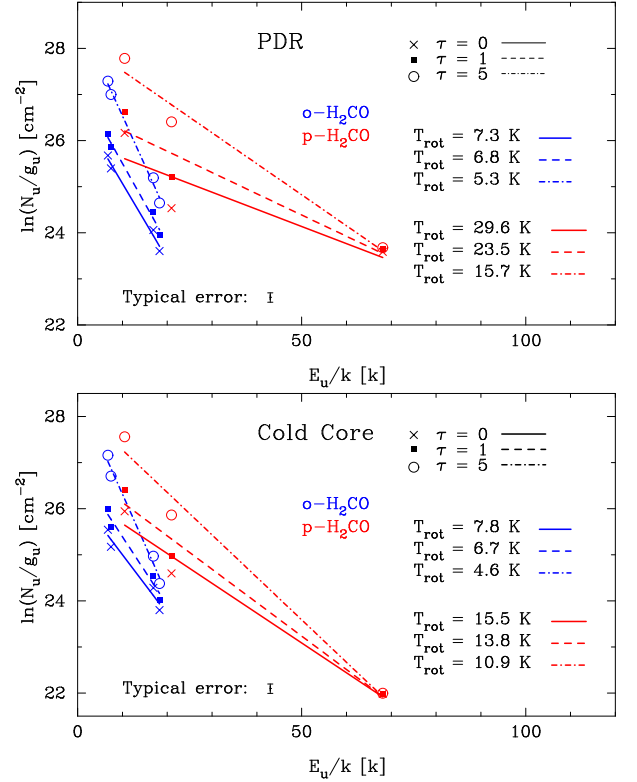


Fig. 5: H<sub>2</sub>CO rotational diagrams corrected for line-opacity effects at the PDR and dense-core position. Rotational temperatures are shown for each considered opacity.

speed of light and  $A_{ul}$  is the Einstein coefficient for spontaneous emission.

Ortho- and para forms of H<sub>2</sub>CO are treated as different species because radiative transitions between them are forbidden. Resulting rotational diagrams are shown in Fig. 5 for three different o-H<sub>2</sub>CO (2<sub>12</sub> – 1<sub>11</sub>) and p-H<sub>2</sub>CO (2<sub>02</sub> – 1<sub>01</sub>) line-opacities ( $\tau = 0, 1$  and  $5$ ). We find column densities of  $N \sim 10^{12} - 10^{13} \text{ cm}^{-2}$ , depending on the opacity. We infer very different rotational temperatures for o-H<sub>2</sub>CO ( $T_{\text{rot}} \sim 4 - 8 \text{ K}$ ) and p-H<sub>2</sub>CO ( $T_{\text{rot}} \sim 10 - 30 \text{ K}$ ), which are also lower than the well-known conditions in the PDR ( $T_{\text{kin}} \sim 60 \text{ K}$ ) and in the dense-core ( $T_{\text{kin}} \sim 20 \text{ K}$ ). This suggests that the gas is far from thermalization, and therefore we used these column densities and rotational temperatures as an input for a more complex analysis to derive the H<sub>2</sub>CO column densities.

### 3.2.3. Radiative transfer models

The critical density of a given collisional partner corresponds to the density at which the sum of spontaneous radiative de-excitation rates is equal to the sum of collisional de-excitation rates ( $\gamma$ ) of a given level

$$n_{cr}(J_{K_a K_c}, T_{\text{kin}}) = \frac{\sum_{J'_{K'_a K'_c}} A(J_{K_a K_c} \rightarrow J'_{K'_a K'_c})}{\sum_{J'_{K'_a K'_c}} \gamma(J_{K_a K_c} \rightarrow J'_{K'_a K'_c}, T_{\text{kin}})}, \quad (5)$$

Formaldehyde lines have high critical densities ( $\sim 10^6 \text{ cm}^{-3}$ , see Table 4) compared to the H<sub>2</sub> density in the Horsehead ( $\sim 10^4 - 10^5 \text{ cm}^{-3}$ ). Because we expect subthermal emission

Table 4: H<sub>2</sub>CO critical densities ( cm<sup>-3</sup>) for three different colliding partners computed for  $T_{\text{kin}} = 60$  K.

$J_{K_a K_c}$	p-H <sub>2</sub>	o-H <sub>2</sub>	He
2 <sub>02</sub>	$7.2 \times 10^5$	$3.6 \times 10^5$	$1.3 \times 10^6$
3 <sub>03</sub>	$1.6 \times 10^6$	$9.9 \times 10^5$	$4.2 \times 10^6$
3 <sub>22</sub>	$5.8 \times 10^5$	$4.7 \times 10^5$	$2.5 \times 10^6$
2 <sub>12</sub>	$3.7 \times 10^5$	$2.5 \times 10^5$	$8.1 \times 10^5$
2 <sub>11</sub>	$4.3 \times 10^5$	$2.2 \times 10^5$	$8.7 \times 10^5$
3 <sub>13</sub>	$9.7 \times 10^5$	$7.0 \times 10^5$	$2.3 \times 10^6$
3 <sub>12</sub>	$1.3 \times 10^6$	$7.9 \times 10^5$	$3.2 \times 10^6$

( $T_{\text{ex}} \ll T_{\text{kin}}$ ) for transitions with high critical densities compared to the H<sub>2</sub> density, we used a nonlocal non-LTE radiative transfer code adapted to the Horsehead geometry to model the observed H<sub>2</sub>CO line intensities (Goicoechea et al. 2006). We used a nonlocal code to take into account the radiative coupling between different cloud positions that might affect the population of the energy levels. The code is able to predict the line profiles. It takes into account line trapping, collisional excitation and radiative excitation by absorption of cosmic microwave background and dust continuum photons. We included 40 rotational levels for o-H<sub>2</sub>CO and 41 rotational levels for p-H<sub>2</sub>CO, where the maximum energy level lies at  $\sim 285$  K for both species. We considered o-H<sub>2</sub>, p-H<sub>2</sub> and He as collision partners with the following collisional excitation rates:

- Collisional rates of o-H<sub>2</sub>CO and p-H<sub>2</sub>CO with He are taken from Green (1991).
- Collisional rates of o-H<sub>2</sub>CO with o-H<sub>2</sub> and p-H<sub>2</sub> from Troscompt et al. (2009) for the first 10 energy levels, *i.e.*  $E_u \leq 50$  K. We complemented these data with He collision rates of Green (1991) scaled to H<sub>2</sub>. Following the new H<sub>2</sub>CO–H<sub>2</sub> collisional rate calculations, we scaled the H<sub>2</sub>CO–He rates by a factor 2.5 instead of the usual  $\sim 1.4$  mass factor (A. Faure priv. communication).
- Collisional rates of p-H<sub>2</sub>CO with o-H<sub>2</sub> and p-H<sub>2</sub> from Troscompt et al., to be submitted.

Results are presented in Fig. 3 for three different column densities. Best matches (see Table 5) are for column densities of  $N(\text{o-H}_2\text{CO}) = 7.2 \times 10^{12}$  cm<sup>-2</sup> and  $N(\text{p-H}_2\text{CO}) = 3.6 \times 10^{12}$  cm<sup>-2</sup> in the PDR position, and  $N(\text{o-H}_2\text{CO}) = 9.6 \times 10^{12}$  cm<sup>-2</sup> and  $N(\text{p-H}_2\text{CO}) = 3.2 \times 10^{12}$  cm<sup>-2</sup> in the dense-core position. In the excitation- and radiative transfer models we adopt an H<sub>2</sub> ortho-to-para ratio of 3 (high-temperature limit), although it is likely that the ortho-to-para ratio is lower in the Horsehead (e.g., Habart et al. 2011). Indeed, the H<sub>2</sub>CO column densities are not sensitive to the change of the H<sub>2</sub> ortho-to-para ratio for the physical conditions of the Horsehead (see Appendix A).

### 3.3. H<sub>2</sub>CO ortho-to-para ratio

The ratio between the column densities of o-H<sub>2</sub>CO and p-H<sub>2</sub>CO provides information about the formation of the molecule, because the characteristic conversion time from one symmetry state to the other is longer than the H<sub>2</sub>CO lifetime (Tudorie et al. 2006). When the molecule forms in the gas-phase, a ratio of 3 is expected, which corresponds to the statistical weight ratio between the ground states of the ortho- and para species. A ratio lower than 3 is expected when the molecule is formed on the surface of cold ( $T_{\text{dust}} \lesssim 20$  K) dust grains (Kahane et al. 1984; Dickens & Irvine 1999). From the derived column densities we

Table 5: Column densities and abundances.

	Molecule	PDR	Dense-core
Column densities [ cm <sup>-2</sup> ]	$N_{\text{H}}$	$3.8 \times 10^{22}$	$6.4 \times 10^{22}$
	$N(\text{o-H}_2\text{CO})$	$7.2 \times 10^{12}$	$9.6 \times 10^{12}$
	$N(\text{p-H}_2\text{CO})$	$3.6 \times 10^{12}$	$3.2 \times 10^{12}$
	$N(\text{HCO})^a$	$3.2 \times 10^{13}$	$< 4.6 \times 10^{12}$
	$N(\text{HD}\text{CO})^b$	-	$1.6 \times 10^{12}$
	$N(\text{o-D}_2\text{CO})^b$	-	$5.1 \times 10^{11}$
Abundances [X] = $\frac{N(\text{X})}{(N(\text{H})+2 N(\text{H}_2))}$	[o-H <sub>2</sub> CO]	$1.9 \times 10^{-10}$	$1.5 \times 10^{-10}$
	[p-H <sub>2</sub> CO]	$9.5 \times 10^{-11}$	$5.0 \times 10^{-11}$
	[HCO]	$8.4 \times 10^{-10}$	$< 7.2 \times 10^{-11}$
	[HD\text{CO}]	-	$2.5 \times 10^{-11}$
	[D <sub>2</sub> CO]	-	$1.6 \times 10^{-11}$

<sup>a</sup> Gerin et al. (2009)

<sup>b</sup> For  $T_{\text{ex}} = 6$  K (LTE).

infer H<sub>2</sub>CO ortho-to-para ratios of  $\sim 2$  in the PDR and of  $\sim 3$  in the dense-core. This suggests that in the dense-core H<sub>2</sub>CO is mainly formed in the gas-phase, whereas in the PDR H<sub>2</sub>CO is formed on the surface of dust grains. Dickens & Irvine (1999) measured H<sub>2</sub>CO ortho-to-para ratios between 1.5 and 2 toward star-forming cores with outflows, and ratios near 3 toward three quiescent cores. Jørgensen et al. (2005) also found an ortho-to-para ratio of 1.6 in the envelopes around low-mass protostars.

### 3.4. HD\text{CO} and D<sub>2</sub>CO column densities

We detected HD\text{CO} and D<sub>2</sub>CO in the dense-core (see two bottom rows in Fig. 4), and we estimated their abundances assuming LTE. For  $T_{\text{ex}} = 6$  K we obtain  $N(\text{HD}\text{CO}) = 1.6 \times 10^{12}$  cm<sup>-2</sup>,  $N(\text{D}_2\text{CO}) = 5.1 \times 10^{11}$  cm<sup>-2</sup> and a D<sub>2</sub>CO ortho-to-para ratio of 1, which translates into relative abundances or fractionation levels  $[\text{HD}\text{CO}]/[\text{H}_2\text{CO}] = 0.11$  and  $[\text{D}_2\text{CO}]/[\text{H}_2\text{CO}] = 0.04$  for the inferred formaldehyde column densities in the dense-core.

Deuterium fractionation can occur in the gas-phase by means of ion-molecule reactions, where D is transferred from HD to other species. High abundances of deuterated molecules compared to the elemental D/H abundance ( $\sim 1.5 \times 10^{-5}$ , Linsky et al. 2006) have been observed in different astrophysical environments, from cold dense cores and hot molecular cores even to PDRs. Pety et al. (2007) found high deuteration ( $[\text{DCO}^+]/[\text{HCO}^+] > 0.02$ ) in the Horsehead dense-core. A pure gas-phase chemical model was able to reproduce the observed fractionation level of HCO<sup>+</sup> for  $T_{\text{kin}} \leq 20$  K. Parise et al. (2009) found high fractionation levels for DCN and HD\text{CO} toward the Orion Bar PDR ( $[\text{XD}]/[\text{XH}] \sim 0.01$ ). They found that these ratios are consistent with pure gas-phase chemistry models where the gas is warm ( $> 50$  K), so the deuterium chemistry is driven mainly by CH<sub>2</sub>D<sup>+</sup>, as opposed to colder regions ( $\lesssim 20$  K) like the Horsehead dense-core, where H<sub>2</sub>D<sup>+</sup> is the main actor. Owing to the low temperature in the core it is likely that a non-negligible fraction of CO is frozen on the dust grains, enhancing the deuterium fractionation.

Another way to form deuterated molecules in cold environments is through D addition or H-D substitution reactions on the surface of dust grains (Hidaka et al. 2009). In the Horsehead core though, desorption from the grain mantles is not efficient in releasing products into the gas-phase (see section 4). It is then more likely that the gas-phase HD\text{CO} and D<sub>2</sub>CO molecules detected here are formed in the gas-phase. Nevertheless, there can still be a considerable amount of deuterated H<sub>2</sub>CO trapped in the ices around dust grains.

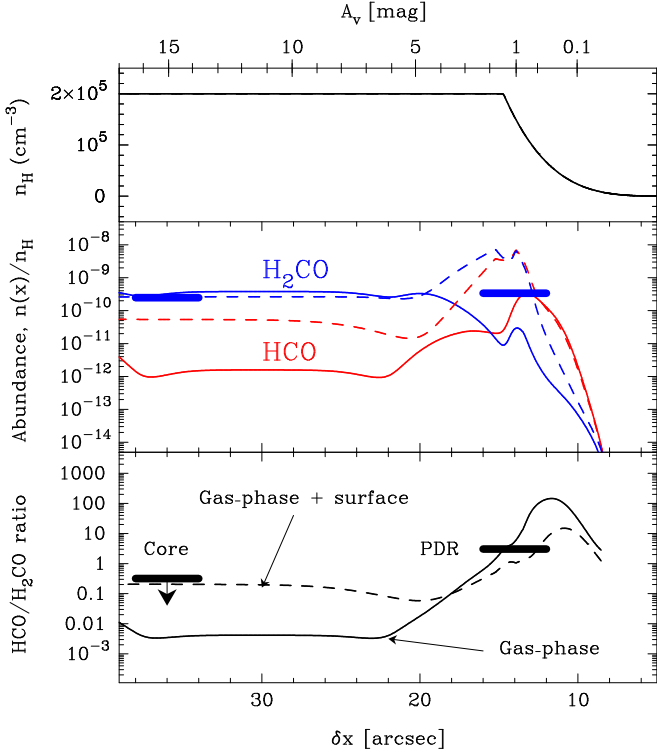


Fig. 6: Photochemical model of the Horsehead PDR. *Upper panel:* PDR density profile ( $n_{\text{H}} = n(\text{H}) + 2n(\text{H}_2)$  in  $\text{cm}^{-3}$ ). *Middle panel:* Predicted abundance (relative to  $n_{\text{H}}$ ) of H<sub>2</sub>CO (blue) and HCO (red). *Lower panel:* Predicted HCO/H<sub>2</sub>CO abundance ratio. In the two bottom panels, models shown as solid lines include pure gas-phase chemistry and models shown as dashed lines include gas-phase as well as grain surface chemistry. The horizontal bars show the measured H<sub>2</sub>CO abundances and abundance ratios.

## 4. H<sub>2</sub>CO chemistry

We used a one-dimensional, steady-state photochemical model (Le Bourlot et al. 1993; Le Petit et al. 2006) to study the H<sub>2</sub>CO chemistry in the Horsehead. The physical conditions have already been constrained by our previous observational studies and we keep the same assumptions for the density profile (displayed in the upper panel of Fig. 6), radiation field ( $\chi = 60$  in Draine units), elemental gas-phase abundances (see Table 6 in Goicoechea et al. 2009b) and cosmic ray ionization rate ( $\zeta = 5 \times 10^{-17} \text{ s}^{-1}$ ).

Unlike other organic molecules like methanol, which can only be efficiently formed on the surface of grains (Tielens & Whittet 1997; Woon 2002; Cuppen et al. 2009), formaldehyde can be formed in both the gas-phase and on the surface of grains. Next, we investigate these two different scenarios.

### 4.1. Pure gas-phase chemistry models

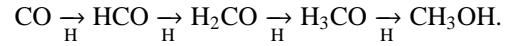
We use the *Ohio State University (osu)* pure gas-phase chemical network upgraded to photochemical studies. We included the photo-dissociation of HCO and of H<sub>2</sub>CO (leading to CO and H<sub>2</sub>) with rates of  $1.1 \times 10^{-9} \exp(-0.8A_V)$  and  $10^{-9} \exp(-1.74A_V) \text{ s}^{-1}$ , respectively (van Dishoeck 1988). We also included the H<sub>2</sub>CO photo-dissociation channel that leads to HCO and H (see e.g., Yin et al. 2007; Troe 2007) with the same rate of the one that

leads to CO and H<sub>2</sub>, and the atomic oxygen reaction with the methylene radical (CH<sub>2</sub>) to explain the high abundance of HCO in the PDR (Gerin et al. 2009).

The predicted HCO and H<sub>2</sub>CO abundance profiles and the HCO/H<sub>2</sub>CO abundance ratio are shown as solid lines in Fig. 6 (middle and lower panel, respectively). The formation of H<sub>2</sub>CO in the PDR and dense-core is dominated by reactions between oxygen atoms and the methyl radical (CH<sub>3</sub>). The destruction of H<sub>2</sub>CO in the PDR is dominated by photo-dissociation, while it is dominated by reactions with ions in the dense-core. The pure-gas phase model satisfactorily reproduces the observed H<sub>2</sub>CO abundance in the dense-core ( $\delta x \sim 35''$ ) but it predicts an abundance in the PDR ( $\delta x \sim 15''$ ) that is at least one order of magnitude lower than the observed value.

### 4.2. Grain chemistry models

We considered the surface chemistry reactions introduced by Stancheva et al. (2002), which include the following sequence of hydrogen addition reactions on CO to form formaldehyde and methanol



We also introduce water formation via hydrogenation reactions of O, OH until H<sub>2</sub>O.

Adsorption, desorption and diffusive reactions were introduced in the Meudon PDR code in the rate equations approach. The corresponding implementation will be described in a specific paper (Le Bourlot et al., to be submitted) and we simply mention the main processes included in the present study. We distinguish between mantle molecules, which may accumulate in several layers (e.g., H<sub>2</sub>O, H<sub>2</sub>CO, CH<sub>3</sub>OH), and light species (e.g., H, H<sub>2</sub>), which stay on the external layer. Photo-desorption can be an efficient mechanism to release molecules to the gas phase in regions exposed to strong radiation fields, as shown recently in laboratory studies (Öberg et al. 2009b,a; Muñoz Caro et al. 2010). Thermal desorption is also introduced. It critically depends on the desorption barrier values, which are somewhat uncertain. Diffusive reactions occur on grain surfaces and the diffusion barriers are assumed to be 1/3 of the desorption energy values. Photodesorption efficiencies have been measured in the laboratory for CO, CO<sub>2</sub>, H<sub>2</sub>O and CH<sub>3</sub>OH. These experiments have shown that all common ices have photodesorption yields of a few  $10^{-3}$  molecules per incident UV photon (Öberg et al. 2007, 2009a,b,c). Therefore, we also take a photo-desorption efficiency of  $10^{-3}$  for those species that have not been studied in the laboratory. We assume in addition that for formaldehyde the two branching ratios toward H<sub>2</sub>CO and HCO+H channels are identical, *i.e.*  $5 \times 10^{-4}$ . Given the high density in the dense-core, the grains are assumed to be strongly coupled to the gas in the inner region, so that their temperatures become equal to 20 K in the dark region, whereas the illuminated dust grains reach temperature values of about 30 K.

The predicted HCO and H<sub>2</sub>CO abundances are shown as dashed lines in Fig. 6. This model reproduces the observed H<sub>2</sub>CO abundance in the dense-core and predicts a similar abundance as the pure gas-phase model. This way, formation on grain surfaces does not contribute significantly to the observed gas-phase H<sub>2</sub>CO abundance in the dense-core. This is because of the low photo-desorption rates in the core caused by the shielding from the external UV field. On the other hand, the H<sub>2</sub>CO abundance can increase by up to three orders of magnitude in the illuminated part of the cloud ( $A_V \lesssim 4$ ) when including the grain

surface reactions. The H<sub>2</sub>CO abundance now even peaks in the PDR, while it peaked in the dense-core in the pure gas-phase model. The model predicts a H<sub>2</sub>CO abundance peak in the PDR that is higher than the observed abundance averaged over the 30m (~ 16"). This limited resolution prevents us from resolving the predicted abundance peak. Interferometric observations are needed to prove the existence of this peak in the PDR.

## 5. Discussion

H<sub>2</sub>CO has been detected in a variety of different astrophysical environments, with a wide range of gas temperatures and densities. It has been detected in diffuse clouds with high abundances (~ 10<sup>-9</sup>), observed in absorption against bright HII regions (e.g., Liszt & Lucas 1995; Liszt et al. 2006). It is not well understood how H<sub>2</sub>CO can be formed and survive in such harsh environments, because gas-phase process cannot compete with the photo-dissociation and dust grain temperatures are too high for molecules to freeze on their surfaces. Roueff et al. (2006) detected absorption lines of H<sub>2</sub>CO at 3.6μm toward the high-mass protostar W33A, and estimated an H<sub>2</sub>CO abundance of ~ 10<sup>-7</sup> where the gas has a temperature of ~ 100 K. Recently, Bergman et al. (2011) found H<sub>2</sub>CO abundances ~ 5 × 10<sup>-9</sup> in the ρ Ophiuchi A cloud core. Abundances of H<sub>2</sub>CO and other more complex molecules toward hot cores and protostars are high. In these regions the gas is dense and hot, so the dust grains also have high temperatures (> 100 K). Therefore, the ice mantles, formed in the cold pre-stellar phase, are completely evaporated. Once these molecules are in the gas-phase, they trigger an active chemistry in the hot gas, forming even more complex molecules (Charnley et al. 1992).

H<sub>2</sub>CO has also been observed in other PDRs. Leurini et al. (2010) detected H<sub>2</sub>CO in the Orion Bar PDR toward both the clump ( $n_{\text{H}} \sim 10^6 \text{ cm}^{-3}$ ) and the inter-clump ( $n_{\text{H}} \sim 10^4 \text{ cm}^{-3}$ ) gas components. They found higher H<sub>2</sub>CO abundances (~ 10<sup>-9</sup> – 10<sup>-7</sup>) than the ones inferred in this work for the Horsehead (~ 10<sup>-10</sup>). Molecules trapped in the ice mantles can be thermally desorbed when the dust grains are warm enough. The dust temperature at which a significant amount of H<sub>2</sub>CO evaporates can be estimated by equating the flux of desorbing molecules from the ices to the flux of adsorbing molecules from the gas (see eq. 5 in Hollenbach et al. 2009). Taking an H<sub>2</sub>CO desorption energy of 2050 K (Garrod & Herbst 2006), we obtain an evaporation temperature of ~ 41 K. In the Orion Bar the dust grains have temperatures of  $T_{\text{dust}} > 55 - 70 \text{ K}$ , so molecules can be desorbed from the icy mantles both thermally and non-thermally. But in the Horsehead PDR dust grains are colder ( $T_{\text{dust}} \sim 20 - 30 \text{ K}$ ), therefore molecules can only be desorbed non-thermally. Hence, the main desorption mechanism in the PDR is photo-desorption. In this respect, the Horsehead PDR offers a cleaner environment to isolate the role of FUV photo-desorption of ice mantles. In the Horsehead dense-core dust grains are also cold (~ 20 K), but photo-desorption is not efficient because the dust is shielded from the external UV field. Cosmic rays can desorb molecules from the ice mantles, but this contribution is not significant because the desorption rates are too low compared to the H<sub>2</sub>CO formation rates in the gas-phase. Both the measured H<sub>2</sub>CO abundance and ortho-to-para ratio agree with the scenario in which H<sub>2</sub>CO in the dense-core is formed in the gas phase with no significant contribution from grain surface chemistry.

We have shown that photo-desorption is an efficient mechanism to form gas-phase H<sub>2</sub>CO in the Horsehead PDR. But, to understand the importance of grain surface chemistry over gas-phase chemistry in the formation of complex organic molecules,

a similar analysis of other molecules, such as CH<sub>3</sub>OH and CH<sub>2</sub>CO, is needed. In particular, CH<sub>3</sub>OH is one of final products in the CO hydrogenation pathway on grain surfaces. It can also form H<sub>2</sub>CO when it is photo-dissociated. Therefore, their gas-phase abundance ratios will help us to constrain their dominant formation mechanism and the relative contributions of gas-phase and grain surface chemistry. Similar studies in different environments will also bring additional information about the relative efficiencies of the different desorption mechanisms.

## 6. Summary and conclusions

We have presented deep observations of H<sub>2</sub>CO lines toward the Horsehead PDR and a shielded condensation less than 40" away from the PDR edge. We complemented these observations with a p-H<sub>2</sub>CO emission map. H<sub>2</sub>CO emission is extended throughout the Horsehead with a relatively constant intensity and resembles the 1.2 mm dust continuum emission. H<sub>2</sub>CO beam-averaged abundances are similar ( $\approx 2 - 3 \times 10^{-10}$ ) in the PDR and dense-core positions. We infer an equilibrium H<sub>2</sub>CO ortho-to-para ratio of ~ 3 in the dense-core, while in the PDR we find a non-equilibrium value of ~ 2.

For the first time we investigated the role of grain surface chemistry in our PDR models of the Horsehead. Pure gas-phase and grain surface chemistry models give similar results of the H<sub>2</sub>CO abundance in the dense-core, both consistent with the observations. This way, the observed gas-phase H<sub>2</sub>CO in the core is formed mainly through gas-phase reactions, with no significant contribution from surface process. In contrast, photo-desorption of H<sub>2</sub>CO ices from dust grains is needed to explain the observed H<sub>2</sub>CO gas-phase abundance in the PDR, because gas-phase chemistry alone does not produce enough H<sub>2</sub>CO. These different formation routes are consistent with the inferred H<sub>2</sub>CO ortho-to-para ratios. Thus, photo-desorption is an efficient mechanism to produce complex organic molecules in the PDR. Because the chemistries of H<sub>2</sub>CO and CH<sub>3</sub>OH are closely linked, we will continue this investigation in a next paper by studying the chemistry of CH<sub>3</sub>OH in detail.

*Acknowledgements.* We thank A. Faure and N. Troscompt for sending us the p-H<sub>2</sub>CO - o-H<sub>2</sub> and p-H<sub>2</sub>CO - p-H<sub>2</sub> collisional rates prior to publication. We thank the referee for a careful reading of the manuscript and interesting comments. VG thanks support from the Chilean Government through the Becas Chile scholarship program. This work was also funded by grant ANR-09-BLAN-0231-01 from the French *Agence Nationale de la Recherche* as part of the SCHISM project. JRG thanks the Spanish MICINN for funding support through grants AYA2009-07304 and CSD2009-00038. JRG is supported by a Ramón y Cajal research contract from the Spanish MICINN and co-financed by the European Social Fund.

## References

- Araya, E., Hofner, P., Goss, W. M., et al. 2007, *ApJS*, 170, 152
- Bergman, P., Parise, B., Liseau, R., & Larsson, B. 2011, *A&A*, 527, 39
- Bisschop, S. E., Jørgensen, J. K., van Dishoeck, E. F., & de Wachter, E. B. M. 2007, *A&A*, 465, 913
- Bowler, B. P., Waller, W. H., Megeath, S. T., Patten, B. M., & Tamura, M. 2009, *AJ*, 137, 3685
- Charnley, S. B., Tielens, A. G. G. M., & Millar, T. J. 1992, *ApJ*, 399, L71
- Cuppen, H. M., van Dishoeck, E. F., Herbst, E., & Tielens, A. G. G. M. 2009, *A&A*, 508, 275
- de Jong, T., Boland, W., & Dalgarno, A. 1980, *A&A*, 91, 68
- Dickens, J. E. & Irvine, W. M. 1999, *ApJ*, 518, 733
- Downes, D., Wilson, T. L., Bieging, J., & Wink, J. 1980, *A&AS*, 40, 379
- Draine, B. T. 1978, *ApJS*, 36, 595
- Garrod, R. T. & Herbst, E. 2006, *A&A*, 457, 927
- Garrod, R. T., Wakelam, V., & Herbst, E. 2007, *A&A*, 467, 1103
- Gerin, M., Goicoechea, J. R., Pety, J., & Hily-Blant, P. 2009, *A&A*, 494, 977

Goicoechea, J. R., Compiègne, M., & Habart, E. 2009a, *ApJ*, 699, L165  
Goicoechea, J. R., Pety, J., Gerin, M., Hily-Blant, P., & Le Boulrot, J. 2009b, *A&A*, 498, 771  
Goicoechea, J. R., Pety, J., Gerin, M., et al. 2006, *A&A*, 456, 565  
Goldsmith, P. F. & Langer, W. D. 1999, *ApJ*, 517, 209  
Green, S. 1991, *ApJS*, 76, 979  
Habart, E., Abergel, A., Boulanger, F., et al. 2011, *A&A*, 527, 122  
Habart, E., Abergel, A., Walmsley, C. M., Teyssier, D., & Pety, J. 2005, *A&A*, 437, 177  
Hassel, G. E., Herbst, E., & Bergin, E. A. 2010, *A&A*, 515, 66  
Hidaka, H., Watanabe, M., Kouchi, A., & Watanabe, N. 2009, *ApJ*, 702, 291  
Hily-Blant, P., Teyssier, D., Philipp, S., & Güsten, R. 2005, *A&A*, 440, 909  
Hollenbach, D., Kaufman, M. J., Bergin, E. A., & Melnick, G. J. 2009, *ApJ*, 690, 1497  
Jørgensen, J. K., Schöier, F. L., & van Dishoeck, E. F. 2005, *A&A*, 437, 501  
Kahane, C., Lucas, R., Frerking, M. A., Langer, W. D., & Encrenaz, P. 1984, *A&A*, 137, 211  
Langer, W. D. & Penzias, A. A. 1990, *ApJ*, 357, 477  
Le Boulrot, J., Pineau Des Forets, G., Roueff, E., & Flower, D. R. 1993, *A&A*, 267, 233  
Le Petit, F., Nehmé, C., Le Boulrot, J., & Roueff, E. 2006, *ApJS*, 164, 506  
Leurini, S., Parise, B., Schilke, P., Pety, J., & Rolfs, R. 2010, *A&A*, 511, 82  
Linsky, J. L., Drainie, B. T., Moos, H. W., et al. 2006, *ApJ*, 647, 1106  
Liszt, H. & Lucas, R. 1995, *A&A*, 299, 847  
Liszt, H. S., Lucas, R., & Pety, J. 2006, *A&A*, 448, 253  
Mangum, J. G., Darling, J., Menten, K. M., & Henkel, C. 2008, *ApJ*, 673, 832  
Mangum, J. G. & Wootten, A. 1993, *ApJS*, 89, 123  
Maret, S., Ceccarelli, C., Caux, E., et al. 2004, *A&A*, 416, 577  
Milam, S. N., Remijan, A. J., Womack, M., et al. 2006, *ApJ*, 649, 1169  
Muñoz Caro, G. M., Jiménez-Escobar, A., Martín-Gago, J. Á., et al. 2010, *A&A*, 522, 108  
Müller, H. S. P., Thorwirth, S., Roth, D. A., & Winnewisser, G. 2001, *A&A*, 370, L49  
Öberg, K. I., Fuchs, G. W., Awad, Z., et al. 2007, *ApJ*, 662, L23  
Öberg, K. I., Garrod, R. T., van Dishoeck, E. F., & Linnartz, H. 2009a, *A&A*, 504, 891  
Öberg, K. I., Linnartz, H., Visser, R., & van Dishoeck, E. F. 2009b, *ApJ*, 693, 1209  
Öberg, K. I., van Dishoeck, E. F., & Linnartz, H. 2009c, *A&A*, 496, 281  
Parise, B., Leurini, S., Schilke, P., et al. 2009, *A&A*, 508, 737  
Penzias, A. A. & Burrus, C. A. 1973, *ARA&A*, 11, 51  
Pety, J. 2005, in *SF2A-2005: Semaine de l'Astrophysique Française*, ed. F. Casoli, T. Contini, J. M. Hameury, & L. Pagani, 721  
Pety, J., Goicoechea, J. R., Hily-Blant, P., Gerin, M., & Teyssier, D. 2007, *A&A*, 464, L41  
Roueff, E., Dartois, E., Geballe, T. R., & Gerin, M. 2006, *A&A*, 447, 963  
Savage, C., Apponi, A. J., Ziurys, L. M., & Wyckoff, S. 2002, *ApJ*, 578, 211  
Snyder, L. E., Buhl, D., Zuckerman, B., & Palmer, P. 1969, *Physical Review Letters*, 22, 679  
Snyder, L. E., Palmer, P., & de Pater, I. 1989, *AJ*, 97, 246  
Stantcheva, T., Shematovich, V. I., & Herbst, E. 2002, *A&A*, 391, 1069  
Tielens, A. G. G. M. & Whittet, D. C. B. 1997, in *IAU Symposium*, Vol. 178, IAU Symposium, ed. E. F. van Dishoeck, 45  
Troe, J. 2007, *Journal of Physical Chemistry A*, 111, 3868  
Troscompt, N., Faure, A., Wiesenfeld, L., Ceccarelli, C., & Valiron, P. 2009, *A&A*, 493, 687  
Tudorie, M., Cacciani, P., Cosléou, J., et al. 2006, *A&A*, 453, 755  
van Dishoeck, E. F. 1988, in *Rate Coefficients in Astrochemistry. Proceedings of a Conference held in UMIST, Manchester, United Kingdom, September 21-24, 1987*. Editors, T.J. Millar, D.A. Williams; Publisher, Kluwer Academic Publishers, Dordrecht, Boston, 1988. ISBN # 90-277-2752-X. LC # QB450 .R38 1988. P. 49, 1988, ed. T. J. Millar & D. A. Williams, 49+  
Walsh, C., Millar, T. J., & Nomura, H. 2010, *ApJ*, 722, 1607  
Woon, D. E. 2002, *ApJ*, 569, 541  
Yin, H.-M., Rowling, S. J., Büll, A., & Kable, S. H. 2007, *J. Chem. Phys.*, 127, 064302  
Young, K. E., Lee, J., Evans, II, N. J., Goldsmith, P. F., & Doty, S. D. 2004, *ApJ*, 614, 252

values for the H<sub>2</sub> ortho-to-para ratio. We show models for an H<sub>2</sub> ortho-to-para ratio of 3 in red (high temperature limit), and we show models for the extreme case where the H<sub>2</sub> ortho-to-para ratio is 0 in green (low temperature limit). The difference between the models is less than 10%, which is within the observational uncertainties and therefore not significant.

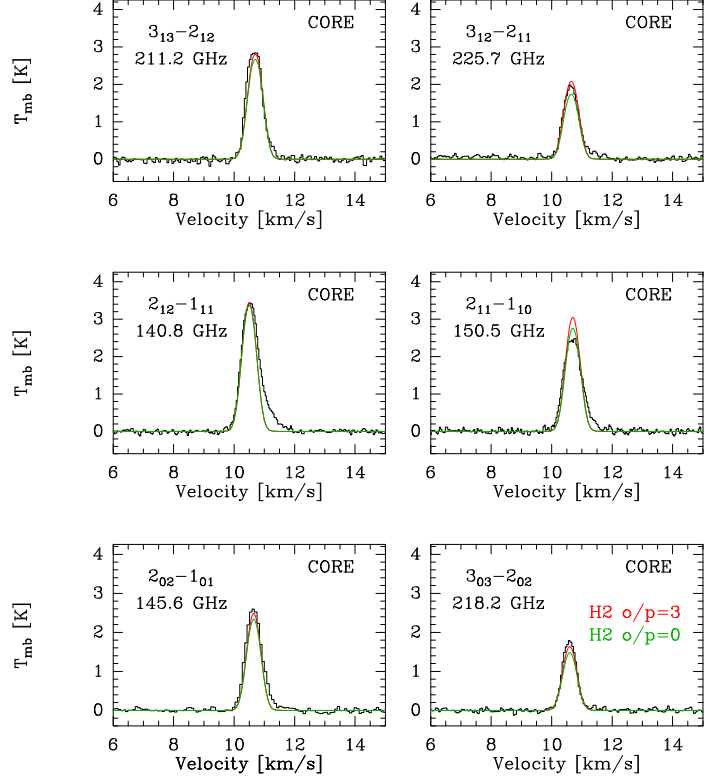


Fig. A.1: Radiative-transfer modeling of H<sub>2</sub>CO lines for the core position in the Horsehead. The two top rows display the ortho lines and the bottom row displays the para lines. The best-match models are given in colors ( $T_{\text{kin}} = 20$  K,  $n(\text{H}_2) = 10^5 \text{ cm}^{-3}$ ,  $N(\text{o-H}_2\text{CO}) = 9.6 \times 10^{12} \text{ cm}^{-2}$ ,  $N(\text{p-H}_2\text{CO}) = 3.2 \times 10^{12} \text{ cm}^{-2}$ ), taking a H<sub>2</sub> ortho-to-para ratio of 3 (red lines) and of 0 (green lines).

## Appendix A: H<sub>2</sub> ortho-to-para ratio

We investigated the influence of the H<sub>2</sub> ortho-to-para ratio adopted in the excitation and radiative transfer models. In Fig. A.1 we show the best-match models for the H<sub>2</sub>CO lines toward the core position in the Horsehead assuming two different